electronics

MDPI

Article

Melt Characteristics of a Deposited Layer on Rail Surface under Different Contact Models for Electromagnetic Launching

Jinming Yao [1,*], Jianbo Bao [2], Jiandong Sun [2], Tengfei Zhang [1] and Qinglei Wang [3]

[1] College of Automation & College of Artificial Intelligence, Nanjing University of Posts and Telecommunications, Nanjing 210003, China; tfzhang@126.com
[2] Nari Group Corporation, Nanjing 211106, China
[3] Jinshan Power Supply Company, Shanghai 200540, China
* Correspondence: yaojinming@njupt.edu.cn

Abstract: Understanding the melting of the deposited layer is crucial for the armature's melting process and sliding electrical contact performance. This study first establishes contact models for both the boundary lubrication state (BLS) and squeezed-film lubrication state (SFLS). A three-dimensional magnetic diffusion model is then constructed to simulate interface current distribution in these contact states. It is discovered that the maximum current density on the surface of the armature shows a decreasing trend as the thickness of the deposited layer grows. Then, a calculation model for the deposited layer's melting thickness under BLS is developed. For SFLS, Reynolds and energy equations are used to construct models for liquid film thickness and the deposited layer's melting thickness. The results indicate that the deposited layer's melting thickness under BLS is significantly greater than that under SFLS. Specifically, the melting thickness decreases with launching displacement in BLS and increases under SFLS. In SFLS, the deposited layer's melting can suppress armature melting, though it remains nearly equivalent to that observed with polished rail. These findings provide a foundation for deposited layer control technology, which is essential for enhancing sliding electric contact performance and launching efficiency.

Keywords: electromagnetic launch; contact state; deposited layer melting; armature melting

check for updates

Citation: Yao, J.; Bao, J.; Sun, J.; Zhang, T.; Wang, Q. Melt Characteristics of a Deposited Layer on Rail Surface under Different Contact Models for Electromagnetic Launching. *Electronics* **2024**, *13*, 4214. https://doi.org/10.3390/electronics13214214

Academic Editor: Andrea Randazzo

Received: 13 September 2024
Revised: 21 October 2024
Accepted: 25 October 2024
Published: 27 October 2024

Copyright: © 2024 by the authors. Licensee MDPI, Basel, Switzerland. This article is an open access article distributed under the terms and conditions of the Creative Commons Attribution (CC BY) license (https://creativecommons.org/licenses/by/4.0/).

1. Introduction

Electromagnetic rail launch (EML) uses electromagnetic force generated by a high-power pulsed high current to drive an armature at high speed in a straight line [1–3].

The armature is a key component in EML, which is mainly responsible for converting electrical energy into kinetic energy to achieve high-speed launching. The electrical contact interface generates a huge interface source, including Joule and friction heat [4,5]. The armature surface material begins to melt under the heating of the interfacial heat source to produce a liquid layer, which eventually solidifies on the rail surface to form a deposited layer [6,7]. The formation process of the liquid layer was described experimentally in [8], where a complete liquid layer is formed at the interface when the line current density is greater than 20 kA/mm. During repeated launches, the armature slides over the deposited layer on the surface of the rail, the surface material of the deposited layer is heated and melts, and the remelted liquid of the deposited layer and the melted liquid of the armature together form an interface liquid layer [9]. When the liquid layer is less able to support the armature–rail interface contact pressure, the interface is in a boundary lubrication contact state [10], and the interface heat source is Joule heat and friction heat [11]. When the carrying capacity of the liquid layer at the interface can support the contact pressure of the armature–rail interface, it is in a fully lubricated contact state, and the interface heat source is mainly Joule heat and viscous heat [12]. The melting characteristics of the deposited layer under different lubricated contact states and its effect on armature melting affect the interface contact performance; maintaining good contact performance is important to

achieve high-frequency and high-efficiency operation of EML [13–16]. Therefore, it is of great significance to study the melting characteristics of the deposited layer and its effect on armature melting under different lubricated contact states in order to deeply understand the wear mechanism of interface melting and ensure the successful launch of EML.

Unfortunately, it is very difficult to observe the formation and action process of the deposited layer during a shot. One can, however, gain considerable insight into the deposits by looking at the materials remaining in the barrel after a launch [17,18]. The deposited layer was characterized by analyzing its topography, morphology, and elemental composition using optical microscopy, optical spectroscopy, energy-dispersive spectroscopy (EDS), and scanning electron microscopy (SEM) [19–24]. The deposits were found to be mainly composed of aluminum. Cooper analyzed the deposited layer after each shot and found that the deposits' thickness increases linearly with the number of shots [21]. The present research work on the deposits was limited to experimental analysis, which looked at the materials remaining in the barrel after launch. Experiment results indicated that aluminum deposits remelted during a shot [23]. However, the published research results have not yet involved any theoretical studies on the remelting properties of deposited layers. Our team explored heat partition at the rail–armature interface with aluminum deposited and preliminarily analyzed for the inhibitory effect of deposited layer melting on armature melting under boundary lubrication conditions [25,26]. How the deposited layers behaved under different contact needs further studies.

Stiffler [27] first established a melting lubrication model where the interface is a parallel gap and considered that the liquid layer generated by armature melting produces a fluid-squeezed film under the squeezing action of the contact surfaces, putting forward a model for calculating the interface melting rate and film thickness under squeezed film lubrication. Stefani et al. [28–30] modified and improved the model for calculating the melting rate and film thickness under squeezed-film lubrication by considering the effects of interface currents and turbulence on the basis of Stiffler's model. The authors in [31] developed a comprehensive lubrication model for the convergent gap liquid layer, incorporating armature tail deformation, and analyzed the armature melting rate. However, the contribution of the deposited layer's melting rate was not taken into account in the calculation of the liquid layer generation velocity for either the parallel gap or convergent gap scenarios. Although the liquid layer may experience deformation of the armature tail due to magnetic and hydraulic pressures, leading to the formation of an evanescent gap shape, the stability of such an evanescent gap liquid layer remains uncertain [32,33]. Consequently, this paper employs the parallel gap-squeezed film lubrication contact model to analyze the melting characteristics of the deposited layer.

In this paper, the boundary lubrication and squeezed film lubrication contact model are established. A three-dimensional magnetic diffusion simulation model is built, and the interface current distribution is simulated and calculated under two contact states. A calculation model for the melting thickness of the deposited layer in the boundary lubrication state is developed based on simulation results of the interface current distribution and considerations of the deposited layer's melting. Additionally, Reynolds and energy equations are formulated for the squeezed-film lubrication state to establish a model for calculating both the film thickness of the liquid layer and the melting thickness of the deposited layer. The deposits' melting characteristics and their inhibition effect on armature melting under different lubrication conditions were obtained. Control technology and revealing the interface melting mechanism are of great significance in the subsequently deposited layer to improve the contact performance of repeated launching.

2. Analytical Model

2.1. Structure of the Railgun

Figure 1a depicts a typical electromagnetic rail launch principle schematic diagram; the launch system comprises parallel rails, an armature, a pulse power source, and additional components. Because the armature and the rail are both made of good conductive metal,

when the power supply is turned on, the pulse current flows into one side of the rail, through the armature, and back into the power supply to form a current circuit. The strong magnetic field created by the pulse current produces a strong electromagnetic force that pushes the current-carrying armature in the high-speed sliding on the surface of the rail.

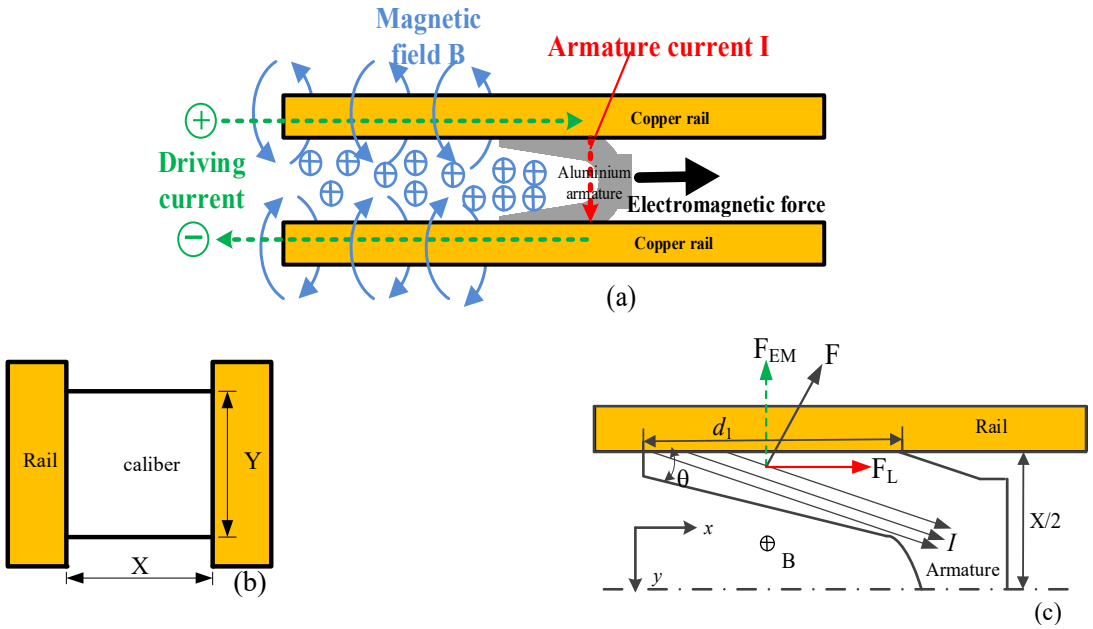


Figure 1. Electromagnetic launch system: (**a**) schematic diagram; (**b**) bore structure; (**c**) armature force analysis.

Figure 1b shows the electromagnetic launching bore structure, where X is the rail spacing, and Y is the armature width. The motion armature moves at high speed under electromagnetic push and friction, and the force analysis of the armature is shown in Figure 1c, where F is the electromagnetic force, F_{EM} is the electromagnetic contact pressure, F_L is the Lorentz force, d_1 is the length of the armature tail, θ is armature tail angle, and U is the armature's speed. If the inductance gradient is L', according to [25], the electromagnetic contact pressure of the armature tail can be obtained as:

$$F_{EM} = \frac{L'I^2(t)}{2}\frac{d_1}{X}\cos\theta \tag{1}$$

If the electromagnetic launch mass is M and the friction coefficient is μ, the armature's sliding speed considering frictional drag force can be calculated as:

$$U(t) = \int_0^t \frac{1}{M}\left[\frac{L'I^2(t)}{2} - 2\cdot\left(\frac{L'I^2(t)}{2}\frac{d_1}{X}\cos\theta\right)\cdot\mu\right]dt \tag{2}$$

The expression for the calculation of armature displacement can be written as:

$$s(t) = \frac{L'}{2M}\left(1 - \frac{2\mu d_1}{X}\cos\theta\right)\int_0^t\left(\int_0^t I^2(t)dt\right)dt \tag{3}$$

The typical driving current waveform of the launcher system is shown in Figure 2. The armature's sliding speed and displacement can be calculated according to expression (2) and the corresponding speed integral calculation; typical curves are pictured in Figure 3. It shows that the current can reach an amplitude of 600 kA in a very short time, and the powerful electromagnetic force pushes the armature to slide at a high speed up to 3000 m/s.

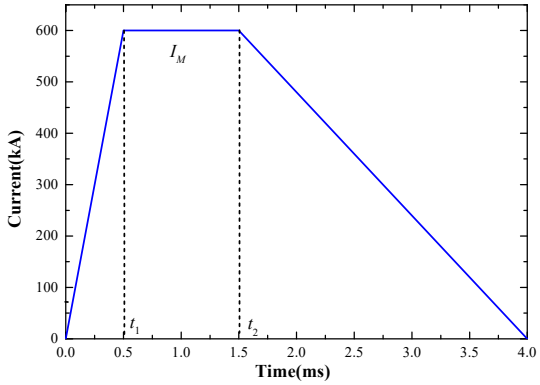


Figure 2. Driving current.

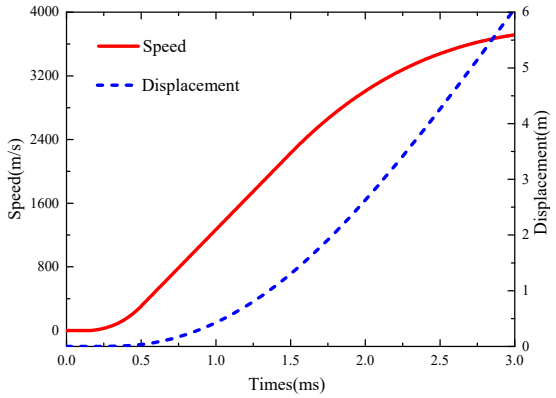


Figure 3. Speed and Displacement curves vs. time.

2.2. Armature-Deposited Layer Rail Contact Model in BLS

When there is less melted aluminum at the interface, as shown in Figure 4b for the melted morphology after launching and Figure 4c for the deposited layer on the rail surface, the deposited layer is relatively thin, and the liquid layer produced by the armature and deposited layer melting is not sufficient to support the armature–rail contact pressure; the interface is in BLS. The armature and rail are in direct contact with each other. In BLS, the sliding electric contact model of the armature's deposited layer is shown in Figure 4a, and the interface heat source is mainly Joule heat and friction heat. Assuming that interface heat loss is not taken into account and that the interface heat source flows into the armature and the deposited layer rails, the heat conducted in the deposited layer causes the deposited layer to melt.

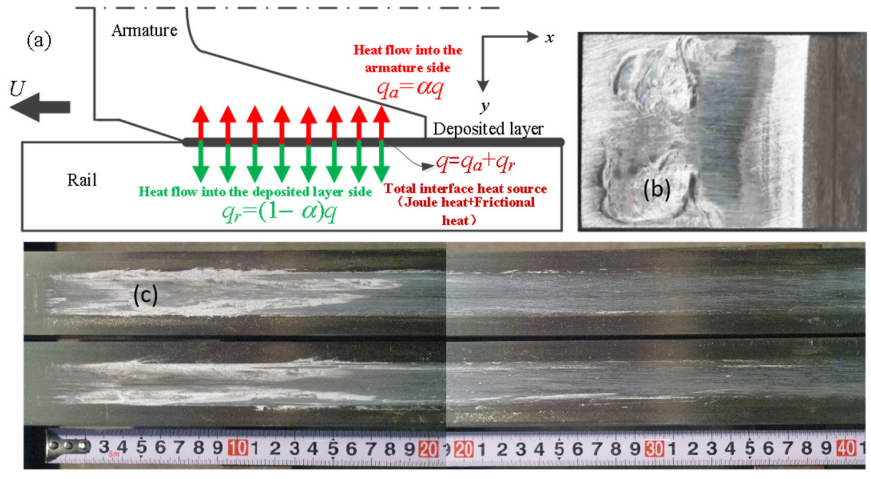


Figure 4. Armature/rail contact model in BLS (**a**) contact model; (**b**) armature melting morphology; (**c**) deposited layer.

For convenience of analysis, assuming that the contact area of the armature–rail remains constant during the sliding process, the interface current density is j, the contact area is A ($A = d_1 Y$), and the contact resistance is R_c, the rate of Joule heat flow generated per unit area can be written as:

$$q_j(t) = j(t)^2 R_c d_1 Y \tag{4}$$

If L' is the inductance gradient, the frictional heat generated per unit area per unit time at the contact interface can be obtained as:

$$q_f(t) = \mu \frac{L' I^2(t)}{2} \frac{U(t)}{XY} \cos\theta \tag{5}$$

The interface Joule heat and frictional heat together constitute the interface heat source during the contact time, which can be approximated as:

$$q(t) = j^2(t) R_c d_1 Y + \mu \frac{L' I^2(t)}{2} \frac{U(t)}{XY} \cos\theta \tag{6}$$

Assuming that the heat partition coefficient on the armature side is α, the heat flow into the armature surface is αq, and the heat flow into the deposited layer is $(1-\alpha)q$. Since the main component of both the armature and the deposited layer material is aluminum, and the thermal parameters of the material are the same, the range of values of the heat partition coefficient can be obtained based on the heat partition calculation method in [26], namely $0.5 \leq 1-\alpha < 1$.

2.3. Armature-Deposited Layer Rail Contact Model in SFLS

With more melted aluminum at the interface, as shown in Figure 5b for the melted morphology after launching of the armature and Figure 5c for the deposited layer on the surface of the rail, the deposited layer is relatively thick, and the liquid layer produced by the armature and deposited layer melting can support the contact pressure of the armature rails; the interface is in SFLS. The armature and rail are not in direct contact, and the interface current enters the liquid layer through the armature surface and finally flows into the deposited layer. The armature-deposited layer rail contact model in SFLS is shown in Figure 5a, in which the interface heat source is mainly Joule heat and viscous heat generated by the liquid layer. Assuming that the interface heat loss and convection effects are not considered, the interface heat sources will flow into the armature and deposited layer.

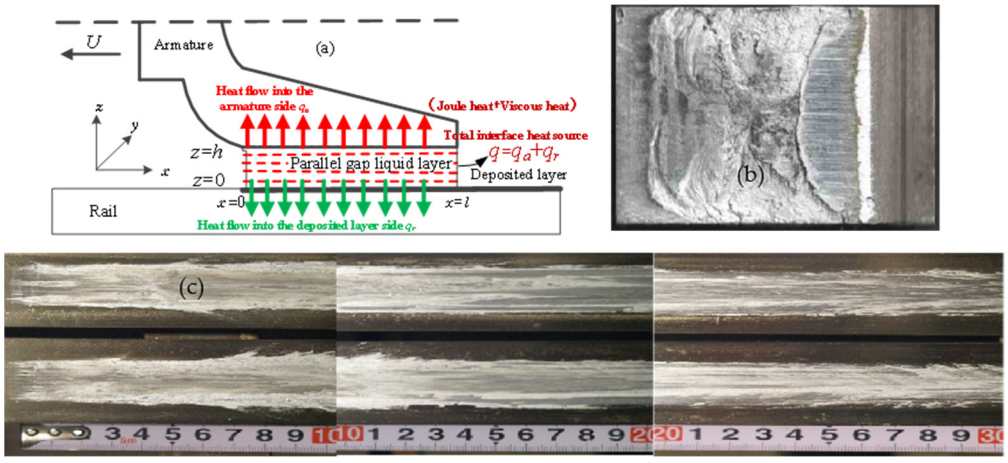


Figure 5. Armature/rail contact model in SFLS (**a**) contact model; (**b**) armature melting morphology; (**c**) deposited layer.

Not considering the armature tail's deformation, assuming that the liquid layer's shape between the armature and rail is as in Figure 5a, the liquid layer's length is l and the

thickness is h. Considering the liquid layer as a parallel gap, i.e.,$\partial h/\partial x = 0$, the Reynolds' equation under the parallel gap can be written as:

$$\nabla^2 P = \frac{12\eta v_m}{h^3} \tag{7}$$

The average pressure P_{av} is [27]:

$$P_{av} = \frac{\eta v_m l^2}{h^3}\left[1 - \frac{192}{\pi^5\beta}\sum_{n=1,3,5}^{\infty} n^{-5}\tanh(n\pi\beta/2)\right] = \frac{\eta v_m l^2}{h^3}\delta \tag{8}$$

where β is the ratio of the long side to the short side of the armature contact surface, v_m is the liquid layer generation rate, which is equal to the interface melting rate, and η is the liquid layer viscosity coefficient.

If $\beta = 1$, then $\delta = 0.421$. Based on the above equation, it can be found that if the contact pressure between the armature and rail is the bore magnetic pressure P_M, then the interface melting rate v_m will maintain the liquid layer's thickness in the parallel gap as:

$$h = \left(\frac{\delta\eta v_m l^2}{P_M}\right)^{1/3} \tag{9}$$

Assuming that the bore cross-sectional area is S, the bore magnetic pressure P_{M} can be approximately written as [33]:

$$P_M = \frac{L' I^2}{2S} \tag{10}$$

In parallel gap conditions, the energy equation for the liquid layer, taking into account the Joule heat, can be written as [27]:

$$k\frac{\partial^2 T}{\partial z^2} + \eta\left(\frac{U}{h}\right)^2 + \frac{j^2}{\sigma} = 0 \tag{11}$$

where j is the current density of the liquid layer, σ is the conductivity of the liquid layer, T is the temperature of the liquid layer, and k is the thermal conductivity.

With boundary conditions: at rail surface $z = 0$, $T = T_r$, and at armature surface $z = h$, $T = T_a = T_m$, the energy equation is solved as:

$$T - T_r = \frac{(T_m - T_r)z}{h} - \left(\frac{\eta U^2}{2kh^2} + \frac{j^2}{2k\sigma}\right)\left(z^2 - zh\right) \tag{12}$$

where T_r is the rail temperature with the deposited layer, T_a is the temperature of the armature, and T_m is the melting temperature of the armature and the deposited layer.

The heat flux from the liquid layer to the armature surface and rail surface, respectively, can be obtained as:

$$\begin{cases} q_a = -k\left.\frac{\partial T}{\partial z}\right|_{z=h} = k(T_r - T_m)/h + \left(\frac{\eta U^2}{2h} + \frac{j^2 h}{2\sigma}\right) \\ q_r = k\left.\frac{\partial T}{\partial z}\right|_{z=0} = -k(T_r - T_m)/h + \left(\frac{\eta U^2}{2h} + \frac{j^2 h}{2\sigma}\right) \end{cases} \tag{13}$$

The total heat flow into the armature and rail, respectively, is:

$$q_a + q_r = \frac{\eta U^2}{h} + \frac{j^2 h}{\sigma} \tag{14}$$

3. Simulation Calculation of Current Density at Armature–Rail Interface

3.1. Current Density Simulation in BLS

Usually the rail material is made of copper, and the armature material is made of aluminum alloy. Since the conduction current of the metal conductor is much larger than the displacement current, the magnetic field of the armature and rail can be regarded as a magnetic quasi-static field. Maxwell's equations in the conductor region can be written as:

$$\begin{cases} \nabla \times \vec{H} = \vec{J}_c \\ \nabla \times \vec{E} = -\frac{\partial \vec{B}}{\partial t} \\ \nabla \cdot \vec{B} = 0 \quad \vec{B} = \mu_0 \vec{H} \\ \nabla \cdot \vec{J}_c = 0 \quad \vec{J}_c = \sigma \vec{E} \end{cases} \tag{15}$$

Introducing vector potential functions $\vec{A}$ and scalar potential functions Φ, the above quasi-static Maxwell's equations can be derived as the magnetic diffusion equation in the conductor region of the electromagnetic launch system:

$$\begin{cases} \vec{B} = \nabla \times \vec{A} \\ \vec{E} = -\frac{\partial \vec{A}}{\partial t} - \nabla \Phi \\ \sigma \frac{\partial \vec{A}}{\partial t} + \nabla \times \frac{1}{\mu_0} \nabla \times \vec{A} + \sigma \nabla \Phi = \vec{J}_c \\ \nabla \cdot (-\sigma \frac{\partial \vec{A}}{\partial t} - \sigma \nabla \Phi) = 0 \end{cases} \tag{16}$$

where J_c is the external conductive current density, μ_0 is the vacuum magnetic permeability, and σ is the electrical conductivity. For the non-conductor region, the conductivity and the applied current density are zero, so the Coulomb norm $\nabla \cdot \vec{A} = 0$ uniquely determines the magnetic vector potential $\vec{A}$ and, thus, the magnetic field in the external region.

At early stages of launches, in order to ensure good contact between the armature and rail, the armature tail usually adopts the interference design. Figure 6 shows the process of interference fit between the armature and rail: Figure 6a is before assembly, and Figure 6b is after assembly. The rail moves toward the armature under the initial mechanical preload by a distance d. A larger d represents a larger initial mechanical preload applied. The solid mechanics module was used in COMSOL Multiphysics® version 6.2 [34,35] to solve the mechanical preload distribution at the armature–rail contact interface.

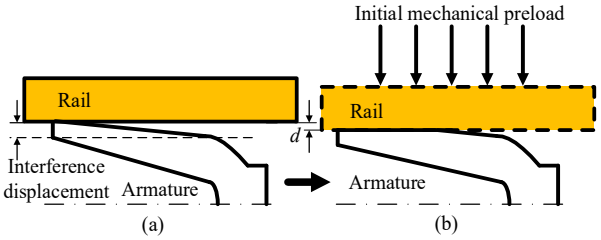


Figure 6. Interference fit between armature and rail (**a**) Before assembly; (**b**) After assembly.

The contact conductance at the armature rail interface in the EM module is calculated as:

$$\sigma_{contact} = 1.25 \frac{2\sigma_a \sigma_r}{\sigma_a + \sigma_r} \frac{m_{asp}}{\sigma_{asp}} \left(\frac{p}{H_c}\right)^{0.95} \tag{17}$$

where σ_a and σ_r are the armature and rail material conductivity, respectively, H_c is the hardness of the softer material, p is the contact pressure, and $\sigma_{contact}$ is the contact conductivity. It can be seen from (17) that the contact pressure affects the contact conductivity, which in turn affects the interface current density distribution.

The three-dimensional simulation model of the armature rail is shown in Figure 7a, and the armature caliber is 20 mm × 20 mm, rail height is 20 mm, rail thickness is 4 mm, and aluminum deposited layer is shown in the blue part of the figure. The rail material is copper, while the armature and deposited layer are made of 6061 aluminum. The material specifications are provided in Table 1. The interference displacement d = 0.8 mm, and the interference contact pressure distribution is obtained in the COMSOL solid mechanics module simulation, as shown in Figure 7b. The simulation of the interface current distribution of the coupled contact pressure can be obtained by importing the results of the contact pressure distribution calculation into the contact conductance calculation model in the COMSOL EM module settings. By setting the thickness of the deposited layer in the COMSOL EM module, the deposited layer's thickness is 0 to simulate no deposited layer rail, and the deposited layer's thickness is set to 500 μm to simulate the deposited layer rail. The simulation obtains the typical current density distribution as shown in Figure 7c,d.

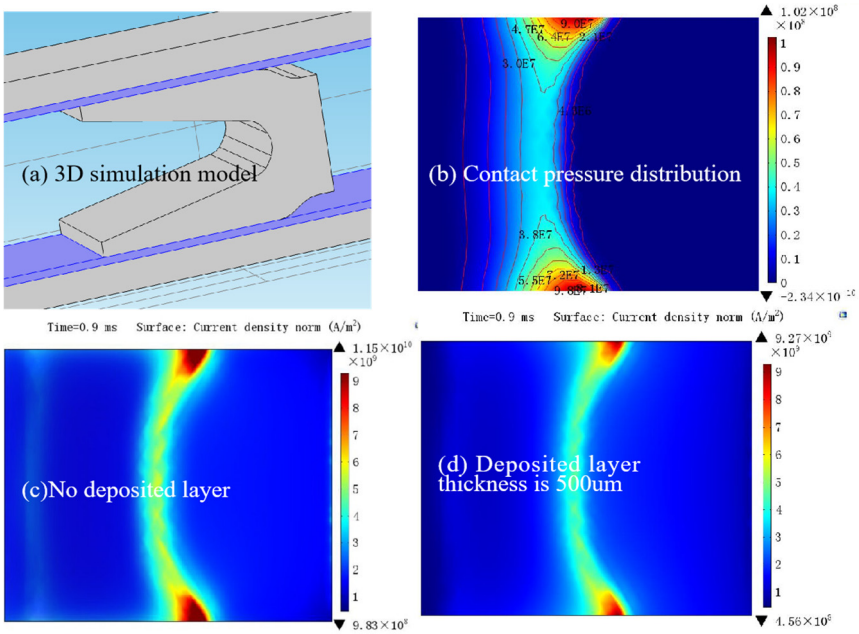


Figure 7. Current simulation in BLS.

Table 1. Material parameters.

Materials	Melting Point (K)	Density (kg/m^3)	Thermal Conductivity (W/m/K)	Specific Heat (J/kg/K)	Conductivity (S/m)	Young's Modulus (Pa)	Poisson's Ratio
Aluminum (6061)	933	2758	170	900	5.4×10^7	90×10^9	0.34
Copper	1358	8950	400	400	1.85×10^7	68.9×10^9	0.33

It can be found that the current distribution on the armature surface is concentrated near the midpoint position of the armature side edge, which is consistent with the contact pressure concentration distribution area. The maximum value of the current density in the case of a 500 μm thick deposited layer is smaller than that in the case of the rail without a deposited layer. Figure 8 shows the current density distribution along the longitudinal direction of the armature at different positions. The current density near the midpoint of the armature side edges is the largest, and further away from the side edges, the position of the current density is smaller. Figure 9 depicts variations in the maximum current density on the surface of the armature with different deposited layer thicknesses, and for the sake of simplicity, the distribution of the current density is taken at the moment of 0.9 ms for the study. It was discovered that the maximum current density on the surface of the armature shows a decreasing trend as the thickness of the deposited layer grows.

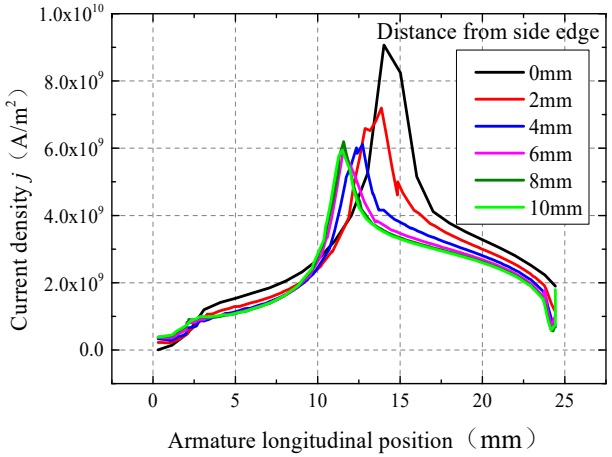


Figure 8. Current distribution along longitudinal direction.

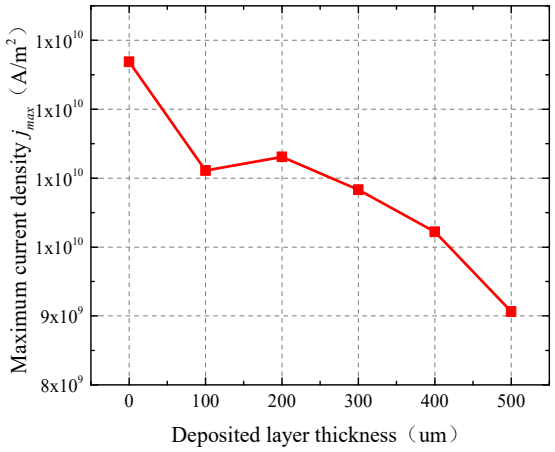


Figure 9. Maximum current along deposited layer thicknesses.

3.2. Current Density Simulation in SFLS

Given that the usual thickness of the liquid layer is significantly lower than the dimensional size of the armature and rail, the liquid layer has no effect on the magnetic field distribution at the armature/rail contact interface. Thus, the magnetic diffusion equations for the rail and armature are as follows:

$$\frac{\partial \vec{B}_r}{\partial t} + U\frac{\partial \vec{B}_r}{\partial x} = \frac{\partial}{\partial x}\left(\frac{1}{\mu_r \sigma_r}\frac{\partial \vec{B}_r}{\partial x}\right) + \frac{\partial}{\partial z}\left(\frac{1}{\mu_r \sigma_r}\frac{\partial \vec{B}_r}{\partial z}\right) \tag{18}$$

$$\frac{\partial \vec{B}_a}{\partial t} = \frac{\partial}{\partial x}\left(\frac{1}{\mu_a \sigma_a}\frac{\partial \vec{B}_a}{\partial x}\right) + \frac{\partial}{\partial z}\left(\frac{1}{\mu_a \sigma_a}\frac{\partial \vec{B}_a}{\partial z}\right) \tag{19}$$

where $\vec{B}_a$, μ_a, and σ_a represent the armature's magnetic induction, permeability, and conductivity, while $\vec{B}_r$, μ_r, and σ_r represent the rail's magnetic induction, permeability, and conductivity. In the normal direction, the armature and rail contact interfaces have equal magnetic induction strengths. Using the above magnetic diffusion equation and boundary conditions, the magnetic field distribution in the armature and rail can be solved in order to determine the current distribution in the armature and rail:

$$J_x = -\frac{1}{\mu_0}\frac{\partial B_y}{\partial z} \tag{20}$$

$$J_z = \frac{1}{\mu_0}\frac{\partial B_y}{\partial x} \tag{21}$$

where J_x and J_z are the current density components in the x and z directions, respectively.

Taking the magnetic diffusion equation as the equation to be solved and the above parameters and current waveform as the solution conditions, the magnetic field distribution of the armature/rail system can be solved after setting it up in COMSOL's Custom Differential Equations module. The magnetic field distribution of the armature/rail contact system during the current rising phase (0–0.5 ms), current flat-topping phase (0.5–1.5 ms), and current falling phase (1.5–4.5 ms) are given in Figure 10. It can be seen that in the current rise stage, the magnetic induction strength gradually increases; in the current flat-top stage, the magnetic field strength reaches the maximum value and remains unchanged, and the bore magnetic field is larger than the internal magnetic field of the conductor. In the current fall stage, the magnetic induction strength begins to decrease.

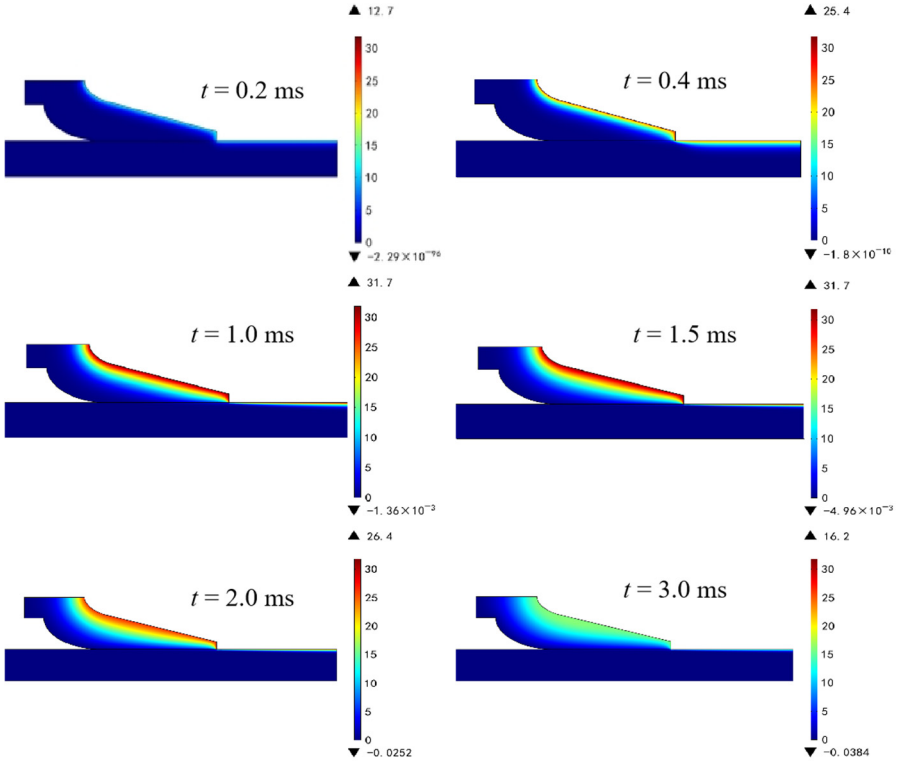


Figure 10. Magnetic field distribution in SFLS.

The current density distribution on the armature/rail contact surface can be obtained by substituting the magnetic field distribution into Equations (20) and (21) for calculation, as shown in Figure 11. Because the metal liquid layer is very thin, it can be assumed that the current flowing through the armature/rail contact surface is the current flowing in the liquid layer.

As seen in the figure, similar to the magnetic field distribution, the current distribution is mostly concentrated at x = 20 mm (armature tail end), where the current density is 2–3 orders of magnitude higher than at other locations. In other regions, the x-direction current in the metal liquid layer is around 10^9 A/m^2, while the z-direction current is about 10^8 A/m^2, which is one order of magnitude less than the x-direction current. The image also shows that the currents in the x and z directions grow increasingly homogeneous with time.

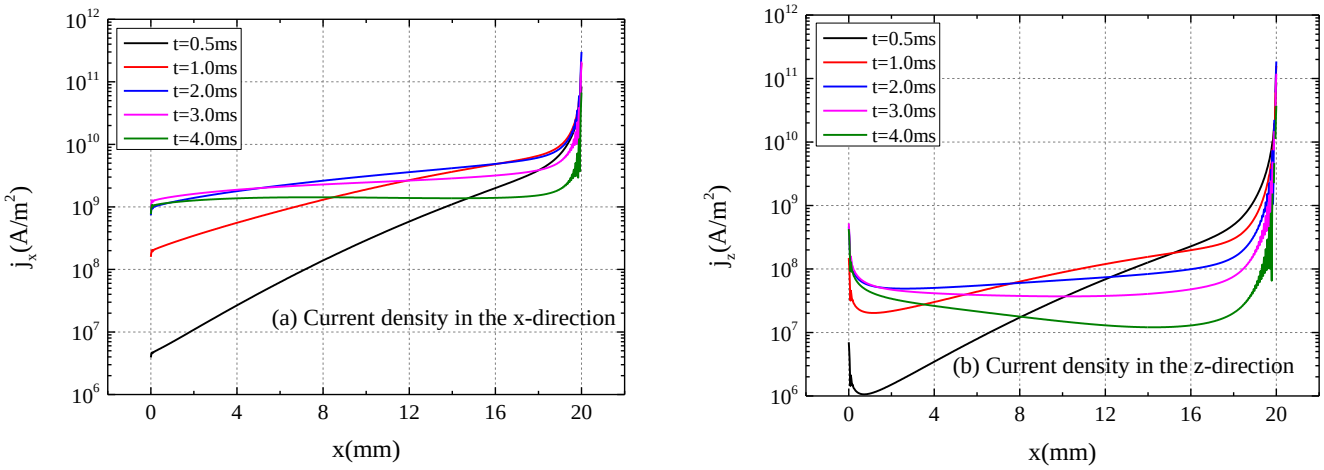


Figure 11. Current distribution in SFLS.

4. Calculated Model for Deposited Layer's Melting Thickness

4.1. Calculated Model for Deposited Layer's Melting Thickness in BLS

The sliding contact process of the armature along the rails with the coated deposited layer is shown in Figure 12. Taking the yellow deposited layer as the research object, the armature starts to contact the yellow deposited layer on the rail at $t = t_{in}$, then leaves at $t = t_{\mathrm{in}} + t_{\mathrm{c}}$, and $t_{\mathrm{c}} = l_a/U$ is the contact time, l_a is the contact length, and U is the armature's sliding speed. During contact time, this sliding contact generates huge frictional and Joule heating at the interface due to friction and the driven current. The heat transfers to the surroundings due to convection and radiation are neglected. It is assumed that there is no heat loss at the sliding interface areas of the armature and deposited rail. Thus, one fraction of the interface heat flows into the contact surface of the armature, and the other fraction of the heat flows into the deposited layer.

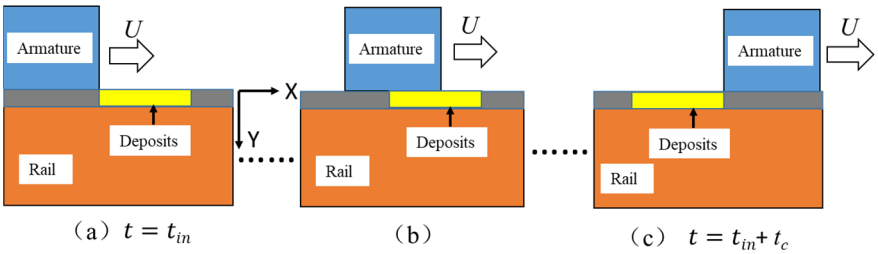


Figure 12. Sliding contact process of armature along the rails with coated deposited layer.

It can be seen that the yellow deposited layer will be heated only during the contact time. From $t = t_{in}$, the deposited layer starts to be heated by the interface heat source and then melts. Once the armature leaves the deposited layer, as shown in Figure 12c, the yellow deposited layer is no longer heated by the heat source.

The heat flowing into the deposited layer is $(1 - \alpha)\, q$. There is a hypothesis that the heat of phase change of the deposit is entirely taken away by the melt wear of deposits. Assuming a volume element with length l, width Y, and the thickness d_0:

$$(c_d\rho_d(T_m - T_0) + h_d)d_0Yl = \int_{t_{in}}^{t_{in}+t_c} Yl(1-\alpha)q(t)dt \tag{22}$$

where h_d is the latent heat of deposits, c_d is the specific heat of deposits, ρ_d is the density of the deposits.

Considering (22), the remelting thickness of the deposited layer during contact time t_c can be expressed as:

$$d_0 = \frac{(1-\alpha)\int_{t_{in}}^{t_{in}+t_c}\left(j^2(t)R_c d_1 Y + \mu\frac{L'I^2(t)}{2}\frac{U(t)}{XY}\cos\theta\right)dt}{\rho_d[H_d + c_d(T_m - T_0)]} \tag{23}$$

where $H_r = h_r/\rho_r$.

If the heat flowing into the deposited layer is the minimum value, meaning $1-\alpha = 0.5$, the minimum value of remelting thickness is d_{min}. Similarly, when the heat flowing into the deposited layer is the maximum, that is $1-\alpha = 1$, the maximum value of the melting thickness is d_{max}. The actual melting thickness d_0 is between d_{min} and d_{max}.

4.2. Calculating the Model for Deposited Layer's Melting Thickness in SFLS

The interface temperature of the deposited layer remains at the melting point temperature T_m after the layer has melted during the contact period, i.e., $T_r = T_m$. This condition is carried over to Equation (13), during which the thermal power transferred from the liquid layer to both the armature and the rails of the deposited layer is equal:

$$q_a = q_r = \frac{\eta U^2}{2h} + \frac{j^2 h}{2\sigma} \tag{24}$$

Assuming the armature melting rate is v_{ma}, the heat balance equation for the armature side, according to the Stiffler model [27], can be expressed as:

$$\left(\frac{\eta U^2}{2h} + \frac{j^2 h}{2\sigma}\right) = \rho_a v_{ma}[H_a + c_a(T_m - T_0)] \tag{25}$$

Assuming the melting rate on the deposited layer side is v_{md}, the heat balance equation for the rail side of the deposited layer can similarly be expressed as:

$$\left(\frac{\eta U^2}{2h} + \frac{j^2 h}{2\sigma}\right) = \rho_d v_{md}[H_d + c_d(T_m - T_0)] \tag{26}$$

where ρ, c, and H represent the material density, specific heat, and latent heat, respectively. In the following table, a denotes the armature, d denotes the deposited layer, and the total liquid layer production rate v_m between the armature rails is the sum of the melting rates of the armature and the deposited layer. Additionally, there are:

$$v_m = v_{ma} + v_{md} \tag{27}$$

The liquid layer production rate v_m introduced into Equation (9) can be expressed as:

$$\frac{P_M h^3}{\delta\eta l^2} = \frac{\frac{\eta U^2}{2h} + \frac{j^2 h}{2\sigma}}{\rho_a[H_a + c_a(T_m - T_0)]} + \frac{\frac{\eta U^2}{2h} + \frac{j^2 h}{2\sigma}}{\rho_d[H_d + c_d(T_m - T_0)]} \tag{28}$$

Considering the effect of turbulence on the liquid layer, the viscous coefficient is adjusted [18], and its equivalent viscous coefficient η_{eff} is:

$$\eta_{eff} = \frac{k_0}{12} h^{3/4} \eta \tag{29}$$

where $k_0 = 0.05(\rho U/\eta)^{\frac{3}{4}}$.

The film thickness of the liquid layer and the total melting rate in the case of turbulent flow are:

$$h = \left(\frac{-B' + \left(B'^2 - 4A'C' \right)^{1/2}}{2A'} \right)^{4/5} \tag{30}$$

$$v_m = \frac{12P_M}{\delta k_0 \eta l^2} h^{9/4} \tag{31}$$

where

$$\begin{cases} A' = \frac{12P_M}{\delta k_0 \eta l^2} \quad B' = -\frac{j^2}{\sigma A_0} \quad C' = -\frac{k_0 \eta U^2}{12 A_0} \\ A_0 = \rho_a [H_a + c_a (T_m - T_0)] \end{cases} \tag{32}$$

Thus, the melting rate of the deposited layer in the case of turbulent flow is:

$$v_{md} = \frac{1}{2} v_m = \frac{6P_M}{\delta k_0 \eta l^2} h^{9/4} \tag{33}$$

The deposited layer's melting thickness during the contact between the liquid layer and the deposited layer is:

$$d_0 = \frac{6P_M}{\delta k_0 \eta l^2} h^{9/4} \frac{d_1}{U} \tag{34}$$

5. Analysis under Different Contact Models

5.1. Deposited Layer Melting Thickness in BLS

The typical armature material is 6061 aluminum, the rail is copper, and the deposited layer material is approximately the same as the armature material. The material parameters are detailed in Table 1. For the analysis, it is assumed that the caliber parameters $X = Y$ are set to 20 mm, d_1 = 20 mm, and M = 30 g. The current waveform is depicted in Figure 2. By varying the current amplitude from 400 kA to 700 kA while keeping other parameters constant, this study examines the minimum melting thickness distribution curve of the deposited layer. The melting thickness distribution at different launch positions is illustrated in Figure 13. The results indicate that the maximum melting thickness of the deposited layer occurs near the starting position. As the launch position advances, the current rapidly attenuates, with the attenuation rate stabilizing during the top phase. Finally, during the current decline phase, the attenuation rate exhibits a nearly linear decreasing trend.

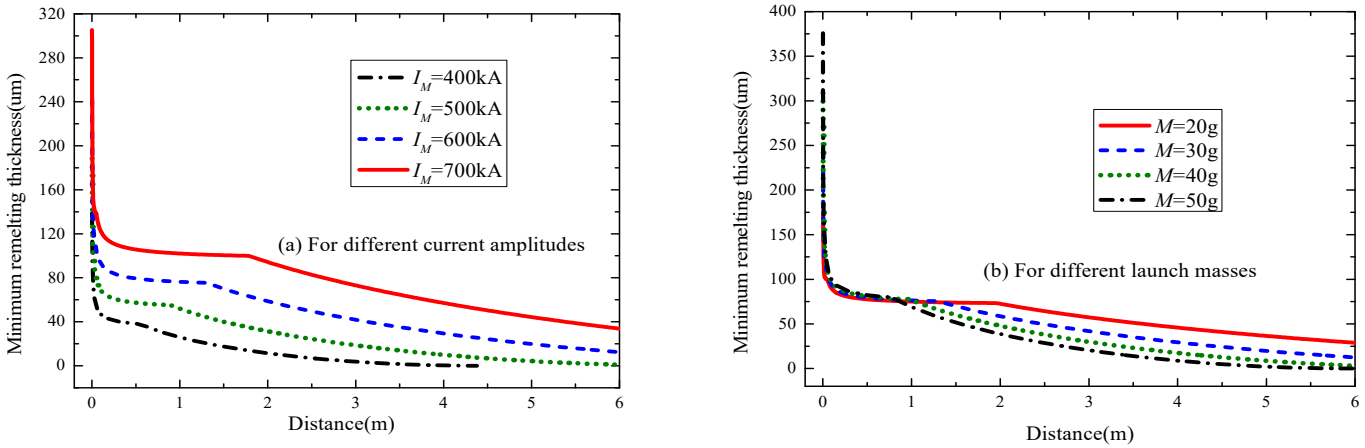


Figure 13. Variation curves of deposited layer melting thickness.

To analyze the impact of varying the launching mass while maintaining a constant current amplitude of 600 kA, the armature sliding speed was adjusted across different launching positions. The minimum melting thickness as a function of displacement under various launching masses is shown in Figure 13b. It was observed that the melting thickness is

greater at the rising edge and the flat top stage. Specifically, larger launching masses result in increased melting thickness at these stages, though the change is not very pronounced. This is attributed to the dominance of interface Joule heating at these stages; a larger mass reduces the armature speed, thus prolonging the duration of Joule heating interaction with the deposited layer, leading to increased melting thickness. Conversely, in the descending stage, larger launching masses result in smaller melting thicknesses of the deposited layer. This occurs because frictional heat becomes the predominant factor in the descending stage. A larger mass reduces the armature velocity, which in turn decreases the frictional heat. Consequently, less heat is absorbed by the deposited layer, resulting in a smaller melting thickness.

5.2. Deposited Layer Melting Thickness in SFLS

When varying the current amplitude from 500 kA to 800 kA while keeping the launch mass constant at 30 g, the curves showing the liquid layer thickness with displacement are presented in Figure 14a. The results indicate that the liquid layer thickness increases gradually with displacement. Although higher current amplitudes lead to a greater liquid layer thickness, the increase is relatively not obvious. Figure 14b illustrates the deposited layer melting thickness as a function of launch displacement for different current amplitudes. It is observed that a higher current results in a greater melting thickness of the deposited layer. However, the melting thickness tends to stabilize as the launch displacement increases and then decreases. The maximum melting thickness of the deposited layer is approximately 38 μm throughout the launching stage, which is significantly smaller than the actual thickness of the deposited layer. Keeping the current amplitude constant at 600 kA, varying the launch mass from 20 g to 50 g affects the armature launch velocity. Figure 15a shows the variation in the film thickness of the liquid layer with displacement for different launch masses. It is evident that a larger launch mass results in a smaller film thickness of the liquid layer. Figure 15b presents the variation in melting thickness of the deposited layer with launch displacement for different launch masses. It is observed that the melting thickness of the deposited layer increases with decreasing mass and tends to stabilize as the launch displacement first increases and then decreases.

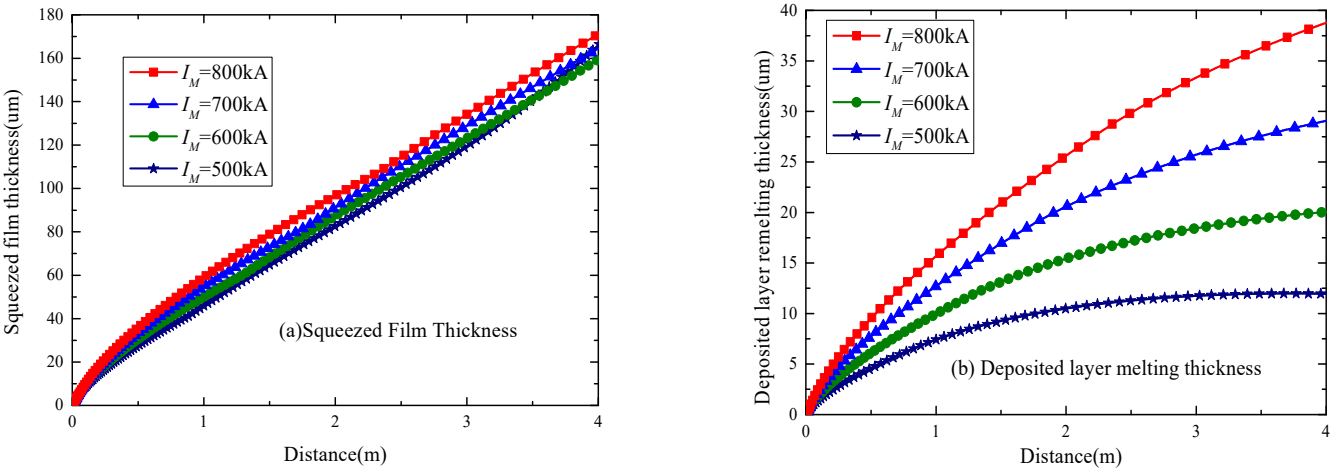


Figure 14. Film thickness of liquid layer and deposited layer melting thickness at different launch currents.

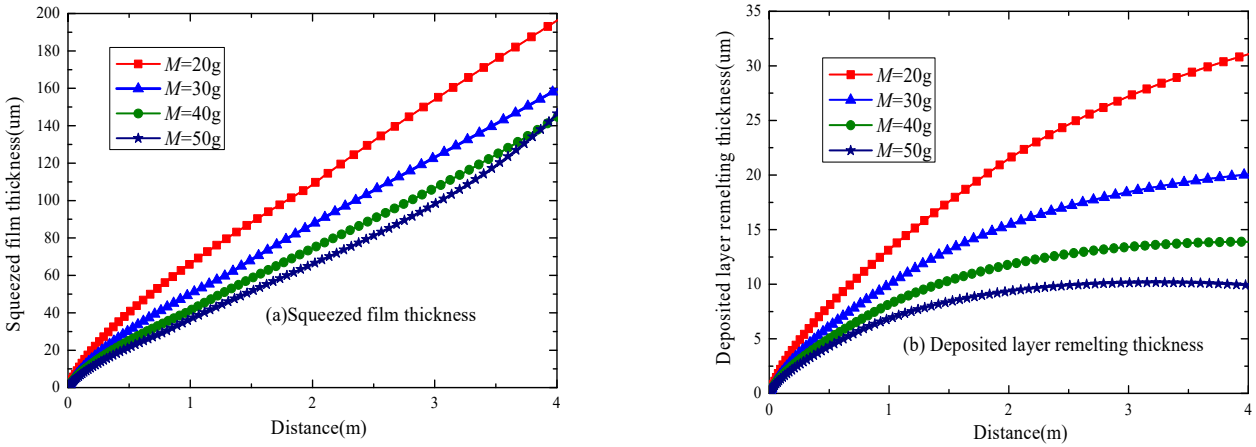


Figure 15. Film thickness of liquid layer and deposited layer melting thickness at different launch speeds.

5.3. Armature Melting Characteristics in SFLS

The corresponding expressions for the liquid layer thickness h and the armature melting rate for the polished rail are solved as follows:

$$h = \left(\frac{-B' + \left(B'^2 - 4A'C' \right)^{1/2}}{2A'} \right)^{4/5} \tag{35}$$

$$v_{ma} = \frac{12P_M}{\delta k_0 \eta l^2} h^{9/4} \tag{36}$$

where

$$\begin{cases} A' = \frac{12\rho_a P_M}{\delta k_0 \eta l^2} [H_a + c_a(T_m - T_0)] \\ B' = -\frac{j^2}{2\sigma} \quad C' = -\frac{k_0 \eta U^2}{24} \end{cases} \tag{37}$$

Figure 16 illustrates the armature melting wear rate and volume for different currents applied to the polished rail. It is observed that both the armature melting rate and volume increase with higher currents. Taking into account the effect of the deposited layer melting, the armature melting rate is:

$$v_{ma} = \frac{\frac{k_0 h^{3/4} \eta U^2}{24h} + \frac{j^2 h}{2\sigma}}{\rho_a [H_a + c_a(T_m - T_0)]} \tag{38}$$

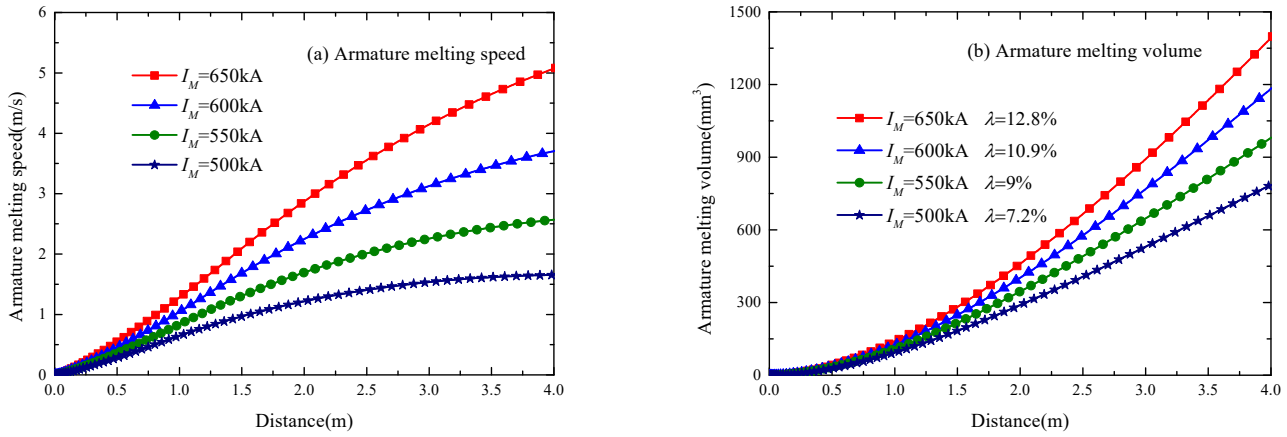


Figure 16. Armature melting for different currents on polished rails.

When considering the effect of deposited layer melting, with the current amplitude and other launch parameters held constant, as in the polished rail scenario, Figure 17 presents the armature melting wear velocity and wear volume under different current amplitudes with deposited layer melting taken into account. It is observed that both the armature melting speed and wear volume increase with launching displacement. However, the armature melting speed and wear volume are reduced compared to the polished rail scenario due to the influence of deposited layer melting, though the difference is not substantial. This suggests that, under squeezed film lubrication conditions, the melting of the deposited layer slightly inhibits armature melting wear but has a minimal overall effect.

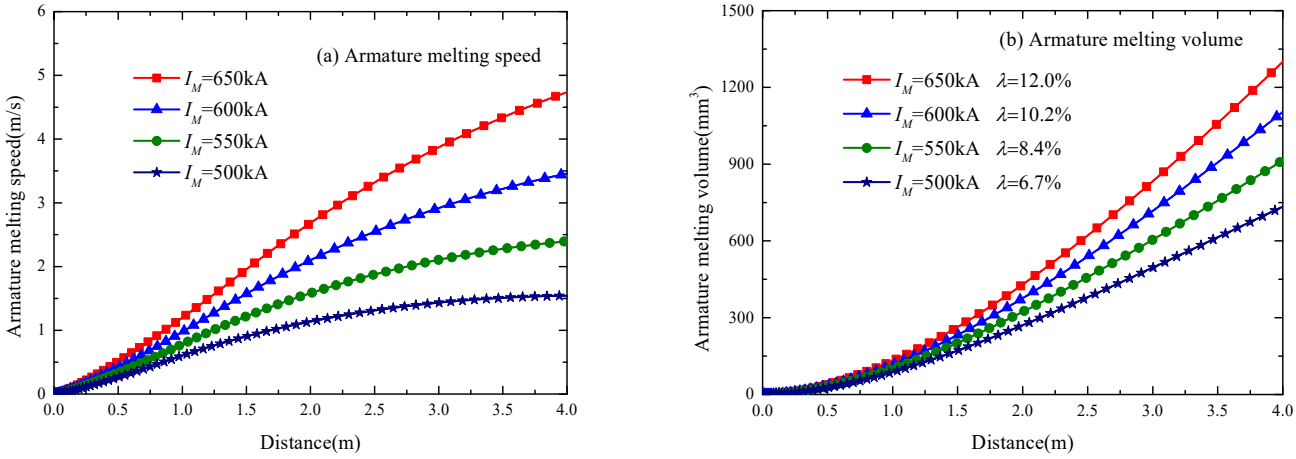


Figure 17. Armature melting at different currents considering melting of deposited layers.

5.4. Comparative Analysis and Discussion

For comparative analysis, Figure 18 illustrates the distribution of melting thickness of the deposited layer under squeezed film lubrication and boundary lubrication conditions, with current and speed held constant. The data reveal that the melting thickness of the deposited layer exhibits a gradual decrease under boundary lubrication, and it shows a gradual increase under squeezed-film lubrication.

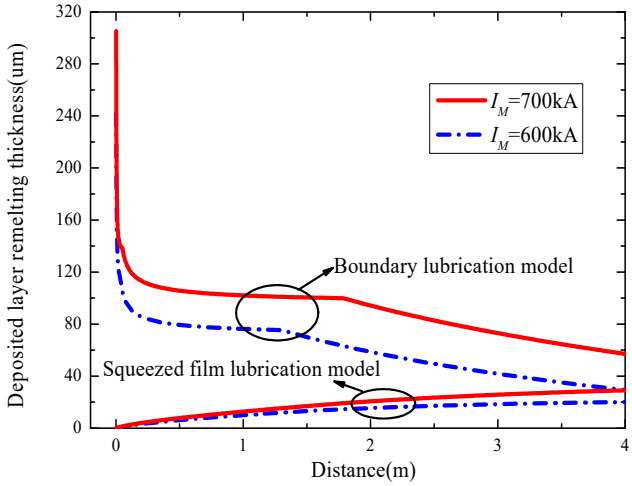


Figure 18. Comparison of deposited layers' melting thickness in BLS and SFLS.

In boundary lubrication, the primary heat sources are Joule heat and friction heat, with Joule heat being predominant during the startup and low-speed stages. During armature startup, the rapid rise in current generates significant Joule heat. Due to the lower speed, the deposited layer is heated for a longer duration, resulting in a larger melting thickness. As speed increases, the heating duration of the deposited layer decreases, which, coupled with

a reduction in current and interface heat source, leads to a significant decrease in melting thickness. Conversely, in squeezed-film lubrication, the main heat source is viscous heat. At low velocities, although the deposited layer is heated for a longer time, the smaller film thickness of the liquid layer and lower viscous heat result in less total heat absorbed by the deposited layer, leading to a smaller melting thickness. As the launching speed increases, the interface viscous heat also increases. Despite the shorter heating duration, the total heat absorbed from the interface rises, causing the melting thickness of the deposited layer to increase gradually. The melting thickness in the boundary lubrication state can reach up to 300 μm, significantly larger than the maximum of 40 μm observed in the squeezed-film lubrication state. This indicates that the interface Joule and friction heat are substantially greater than the viscous heat in the liquid layer, highlighting the lubricating effect of the liquid layer.

6. Conclusions

During repeated launches, the armature slides over the deposited layer on the rail's surface. The deposited layer, together with the armature surface material, is heated and begins to melt, forming a liquid layer. The interface will be in either a boundary lubrication state (BLS) or squeezed-film lubrication state (SFLS), depending on the liquid layer carrying capability and contact pressure. A three-dimensional magnetic diffusion simulation model is built, and the interface current distribution is simulated and calculated. Considering the interface current distribution and melting of the deposited layer, the calculation models have been established for the melting thickness under BLS and SFLS. Deposits' melting characteristics and their inhibition effect on armature melting under different lubrication conditions were also obtained. The key findings are summarized as follows:

(1) The maximum value of the current density in the 500 μm thickness case of the deposited layer is smaller than that in the case of the rail without a deposited layer. As the thickness of the deposited layer increases, the maximum current density on the surface of the armature shows a decreasing trend.
(2) The melting thickness in the boundary lubrication state can reach up to 300 μm, significantly larger than the maximum of 40 μm observed in the squeezed-film lubrication state. This indicates that the interface Joule and friction heat are substantially greater than the viscous heat in the liquid layer, indicating that the liquid layer exhibits a lubrication effect.
(3) Under boundary lubrication conditions, the melting thickness of the deposited layer decreases as the launching displacement increases, whereas under squeezed-film lubrication conditions, the melting thickness increases with greater launching displacement.
(4) In the squeezed-film lubrication scenario, the deposited layer's melting can suppress armature melting, though it remains nearly equivalent to that observed with the polished rail.

These findings revealed the melting behavior of the deposited layer under different contact states, providing a theoretical basis for deeply understanding the wear mechanism of interface melting and deposited layer control technology, which is essential for ensuring the successful launch of EML. It also provides favorable assistance for the subsequent evolution mechanism of the thickness of the deposited layer and the influence of the deposited layer on the melting of the armature.

Author Contributions: Conceptualization, J.Y.; data curation, J.B.; formal analysis, J.S.; investigation, Q.W.; methodology, J.Y.; project administration, T.Z.; resources, J.Y.; software, J.B.; supervision, T.Z.; validation, J.S.; visualization, Q.W. and J.Y.; writing–original draft, J.Y.; writing–review and editing, J.Y. scientific research, J.Y. All authors have read and agreed to the published version of the manuscript.

Funding: This work was supported in part by the National Natural Science Foundation of China under Grant 52207009 and Grant 62073173 and in part by the Key Research & Development Plan of Jiangsu Province, China, under Grant BE2023838.

Data Availability Statement: The data presented in this study are available on request from the corresponding author.

Acknowledgments: The authors would like to thank their teachers, friends, and other colleagues for their discussions on simulation and comments on this paper.

Conflicts of Interest: Author Jianbo Bao and Jiandong Sun were employed by the company Nari Group Corporation (State Grid Electric Power Research Institute). Author Qinglei Wang was employed by the company Jinshan Power Supply Company, State Grid Shanghai Electric Power Company. The remaining authors declare that the research was conducted in the absence of any commercial or financial relationships that could be construed as a potential conflict of interest.

References

1. Ma, W.M.; Lu, J.Y. Research progress and challenges of electromagnetic launch technology. *Trans. China Electrotech. Soc.* **2023**, *38*, 3943–3959.
2. Zhang, P.; Shu, T.; Li, T. Electromagnetic Characteristics Analysis of Quadrupole Compound Orbital Electromagnetic Launcher with Different Configurations. *Electronics* **2022**, *11*, 2650. [CrossRef]
3. Lin, Z.Q.; Chen, G.M.; Xu, L.L. Research on the application of electromagnetic launch technology in missile weapon systems. *Aerodyn. Missile J.* **2020**, *7*, 67–71.
4. Du, X.; Liu, S.; Guan, J. Design and Experimental Study of a Curved Contact Quadrupole Railgun. *Electronics* **2022**, *11*, 3108. [CrossRef]
5. Zhang, J.W.; Lu, J.Y.; Tan, S.; Zhang, Y.; Li, B. A magnetic diffusion model of electromagnetic launcher considering initial contact pressure. *Trans. China Electrotech. Soc.* **2022**, *37*, 488–495.
6. Chen, Y.; Xu, W.D.; Yuan, W.Q.; Zhao, Y.; Yan, P.; Lan, G.F. Sliding Electrical Contacts Between Aluminum Armature and Different Material Rails in Railgun. *High Volt. Eng.* **2013**, *39*, 937–942.
7. Kang, L.; Wang, X.; Liu, Z.Y.; Yuan, Z.; Lin, Y.; Liang, W.; Yao, P. Investigation on wear mechanism and electrical contact performance of CuCrZr alloy rail surfaces for high-speed sliding electrical contact. *Lubr. Eng.* **2024**, *49*, 8–14.
8. Tang, L.L. Experimental and Theoretical Study on Liquid Metal Film Characteristic of Armature/Rail Contact Interface in an Electromagnetic Launching. Ph.D. Thesis, Huazhong University of Science and Technology, Wuhan, China, 2015.
9. Watt, T.J.; Clay, C.E.; Bassett, P.M.; Bourell, D.L. The effect of surface indentations on gouging in railguns. *Wear* **2014**, *310*, 41–50. [CrossRef]
10. Tian, X.; Kennedy, F.E. Contact Surface Temperature Models for Finite Bodies in Dry and Boundary Lubricated Sliding. *J. Tribology. Trans. ASME* **1993**, *115*, 411–418. [CrossRef]
11. Ruan, J.H.; Chen, L.X.; Xia, S.G.; Wang, Z.J.; Li, L.D. Review of current distribution characteristics of electromagnetic railguns. *J. Electrotech. Technol.* **2020**, *35*, 4423–4431.
12. Ruan, J.H.; Chen, L.X.; Wang, Z.J.; Li, C.X.; Wu, P.F.; Xia, S.G. Transition Mechanism Based on Load Imbalance of Liquid Metal Film. *IEEE Trans. Plasma Sci.* **2020**, *48*, 3720–3726. [CrossRef]
13. Chen, L.X.; Xu, X.; Wang, Z.J.; Xu, J.; You, P.; Lan, X. Melting Distribution of Armature in Electromagnetic Rail Launcher. *IEEE Trans. Plasma Sci.* **2023**, *51*, 234–242. [CrossRef]
14. Wen, R.; Li, P.; Wang, H. Investigation of the Distribution Problem in the Operating State of an Electromagnetic Railgun: Radio Fuse Disturbance, Field Characteristics, and Susceptible. *Electronics* **2023**, *12*, 2914. [CrossRef]
15. Zhai, X.F.; Li, X.H.; Liu, H.; Peng, Z. Research on circuit model and launch efficiency of electromagnetic rail launch system. *Trans. China Electrotech. Soc.* **2023**, *38*, 2841–2849.
16. Du, P.P.; Lu, J.Y.; Li, X.P.; Feng, J.H.; Li, K. Interior ballistic characteristics of electromagnetic rail launcher considering the dynamic characteristics of real launcher. *IEEE Trans. Ind. Electron.* **2021**, *68*, 6089–6096. [CrossRef]
17. Li, S.Z.; Cao, R.G.; Zhou, Y. Performance Analysis of Electromagnetic Railgun Launch System Based on Multiple Experimental Data. *IEEE Trans. Plasma Sci.* **2019**, *47*, 524–534. [CrossRef]
18. Gee, R.M.; Persad, C. The response of different copper alloys as rail contacts at the breech of an electromagnetic launche. *IEEE Trans. Magn.* **2001**, *37*, 263–268. [CrossRef]
19. Persad, C. Railgun Tribology—Chemical Reactions Between Contacts. *IEEE Trans. Magn.* **2007**, *43*, 391–395. [CrossRef]
20. Meger, R.A.; Cooper, K.; Jones, H. Analysis of rail surfaces from a multishot railgun. *IEEE Trans. Magn.* **2005**, *41*, 211–213. [CrossRef]
21. Cooper, K.P.; Jones, H.; Meger, R.A. Analysis of railgun barrel materials. *IEEE Trans. Magn.* **2007**, *43*, 120–125. [CrossRef]
22. Meger, R.A. EM gun bore life experiments at Naval research laboratory. *IEEE Trans. Plasma Sci.* **2012**, *41*, 1533–1537. [CrossRef]
23. Watt, T.; Stefani, F.; Crawford, M. Investigation of damage to solid-armature railguns at startup. *IEEE Trans. Magn.* **2007**, *43*, 214–218. [CrossRef]
24. Watt, T.; Motes, D.T. The Effects of Surface Coatings on the Onset of Rail Gouging. *IEEE Trans. Plasma Sci.* **2011**, *39*, 168–173. [CrossRef]
25. Yao, J.M.; Sun, J.D.; Bao, J.B.; Zhang, T.F. Study on Suppressing Effect of Deposits on Armature Melting at Sliding Electrical Contact Interfaces. *Trans. China Electrotech. Soc.* **2024**, *39*, 5958–5968.

26. Yao, J.; Fu, Q. Heat Partition Process at Sliding Electrical Contact Interfaces with High-Speed and Large Current. *Trans. China Electrotech. Soc.* **2024**, *39*, 5497–5507.
27. Stiffler, A.K. Friction and Wear with a Fully Melting Surface. *Trans. ASME J. Tribol.* **1984**, *106*, 416–419. [CrossRef]
28. Kothmann, R.E.; Stefani, F. A Thermal Hydraulic Model of Melt-Lubrication in Railgun Armatures. *IEEE Trans. Magn.* **2001**, *37*, 86–91. [CrossRef]
29. Merrill, R.; Stefani, F. A Turbulent Melt-Lubrication Model of Surface Wear. *IEEE Trans. Magn.* **2005**, *41*, 414–419. [CrossRef]
30. Thiagarajan, V.; Hsieh, K.T. A magnetofluid mechanical model to describe rail–armature interface phenomena. *IEEE Trans. Magn.* **2007**, *43*, 198–203. [CrossRef]
31. Yao, J.M.; Xia, S.G.; Chen, L.X.; He, J.J. Hydrodynamic Lubrication of a Liquid Conducting Film Controlled by Magnetic Pressure at Rail-Armature Interface. *IEEE Trans. Plasma Sci.* **2018**, *46*, 1035–1039. [CrossRef]
32. Yao, J.M.; Chen, L.X.; Xia, S.G.; He, J.J. Stability Analysis of Hydrodynamic Lubrication of a Liquid Conducting Film at Rail-armature Interface. *IEEE Trans. Plasma Sci.* **2019**, *47*, 2250–2255. [CrossRef]
33. Yao, J.M.; Xia, S.G.; Chen, L.X.; He, J.J. Analysis of Hydrodynamic Lubrication Considering the Self-acceleration of a Liquid Conducting Film at Rail-armature Interface. *IEEE Trans. Plasma Sci.* **2019**, *47*, 2256–2263. [CrossRef]
34. Yao, J.M.; Chen, L.X.; Xia, S.G.; He, J.J. The Effect of Current and Speed on Melt Erosion at Rail-Armature Contact in Railgun. *IEEE Trans. Plasma Sci.* **2019**, *47*, 2302–2308. [CrossRef]
35. Pei, C.G.; Liu, G.Z.; Jin, Y.X.; Yuan, Z.K.; Wang, D.W. Dynamic analysis of electromagnetically launched integrated projectiles based on COMSOL. *J. Gun Launch Control.* **2024**, *45*, 104–112.

Disclaimer/Publisher's Note: The statements, opinions and data contained in all publications are solely those of the individual author(s) and contributor(s) and not of MDPI and/or the editor(s). MDPI and/or the editor(s) disclaim responsibility for any injury to people or property resulting from any ideas, methods, instructions or products referred to in the content.